Published in final edited form as:

*ACS Nano*. 2017 January 24; 11(1): 927–937. doi:10.1021/acsnano.6b07525.

# Theranostic Liposomes with Hypoxia-Activated Prodrug to Effectively Destruct Hypoxic Tumors Post-Photodynamic Therapy

**Liangzhu Feng**[†,‡], **Liang Cheng**[†,§], **Ziliang Dong**[†], **Danlei Tao**[†], **Todd E. Barnhart**[§], **Weibo Cai**[*,§], **Meiwan Chen**[*,‡], and **Zhuang Liu**[*,†]

[†]Institute of Functional Nano & Soft Materials (FUNSOM), Jiangsu Key Laboratory for Carbon-Based Functional Materials and Devices, Soochow University, Suzhou 215123, China

[‡]State Key Laboratory of Quality Research in Chinese Medicine, Institute of Chinese Medical Sciences, University of Macau, Macau 999078, China

[§]Departments of Radiology and Medical Physics, University of Wisconsin-Madison, Madison, Wisconsin 53705, United States

## Abstract

Photodynamic therapy (PDT), a noninvasive cancer therapeutic method triggered by light, would lead to severe tumor hypoxia after treatment. Utilizing a hypoxia-activated prodrug, AQ4N, which only shows toxicity to cancer cells under hypoxic environment, herein, a multipurpose liposome is prepared by encapsulating hydrophilic AQ4N and hydrophobic hexadecylamine conjugated chlorin e6 (*h*Ce6), a photosensitizer, into its aqueous cavity and hydrophobic bilayer, respectively. After chelating a $^{64}$Cu isotope with Ce6, the obtained AQ4N-$^{64}$Cu-*h*Ce6-liposome is demonstrated to be an effective imaging probe for *in vivo* positron emission tomography, which together with *in vivo* fluorescence and photoacoustic imaging uncovers efficient passive homing of those liposomes after intravenous injection. After being irradiated with the 660 nm light-emitting diode light, the tumor bearing mice with injection of AQ4N-*h*Ce6-liposome show severe tumor hypoxia, which in turn would trigger activation of AQ4N, and finally contributes to remarkably improved cancer treatment outcomes *via* sequential PDT and hypoxia-activated chemotherapy. This work highlights a liposome-based theranostic nanomedicine that could utilize tumor hypoxia, a side effect of PDT, to trigger chemotherapy, resulting in greatly improved efficacy compared to conventional cancer PDT.

## Graphical Abstract

[*]Corresponding Authors: wcai@uwhealth.org. mwchen@umac.mo. zliu@suda.edu.cn.

**ORCID**

Zhuang Liu: 0000-0002-1629-1039

The authors declare no competing financial interest.

Supporting Information

The Supporting Information is available free of charge on the ACS Publications website at DOI: 10.1021/acsnano.6b07525. The synthesis process and MAIDI-TOF spectrum of *h*Ce6, *in vitro* release profile, and intracellular metabolic profile of AQ4N; relative cell viabilities of cells treated with free AQ4N under both normoxic and hypoxic condition; *in vitro* photodynamic toxicity of *h*Ce6; radiolabeling yield and stability of $^{64}Cu^{2+}$ on AQ4N-*h*Ce6-liposomes; cytotoxicity of Cu-*h*Ce6-liposomes and PA imaging of AQ4N-*h*Ce6-liposomes (PDF)

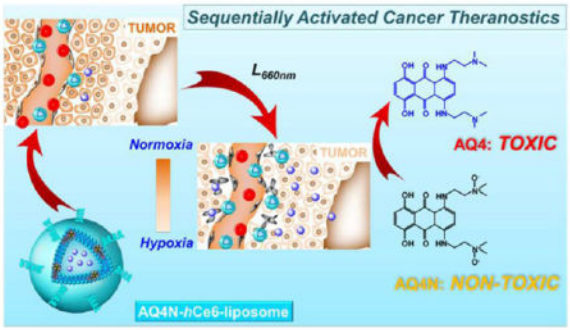


**Keywords**

liposomes; tumor hypoxia; multimodal imaging; photodynamic therapy; hypoxia-activated therapy

Tumor hypoxia, a characteristic feature of most solid tumors stemming from their hostile microenvironments (*e.g.*, heterogeneous tumor growth, abnormal vasculatures), has been found to be one of the key reasons for the poor prognosis of many cancer therapeutics.[1–3] After considering those impediments for efficient cancer treatment, unlike many proposed strategies trying to relieve tumor hypoxia, some pioneering studies have demonstrated an opposite strategy for more effective and selective cancer therapy by utilizing the tumor hypoxia.[4–11] Among them, hypoxia-activated prodrugs, which could be converted from nontoxic prodrug molecules to toxic drugs by reduction under hypoxia, have received a great deal of research interests.[12–19] However, the use of hypoxia-activated prodrugs alone usually could not offer a satisfied antitumor effect, as they are ineffective toward tumor cells nearby tumor vasculatures with sufficient oxygen supply. Therefore, it might be a promising strategy to combine hypoxia-activated chemotherapy with other therapeutics for cancer treatment.

Photodynamic therapy (PDT), which utilizes singlet oxygen generated from photosensitizers under light illumination to kill cells, has attracted tremendous attention for the treatment of many diseases including cancers, owing to its noninvasive feature and high selectivity.[19–27] Unfortunately, the therapeutic outcome of PDT is severely affected by the tumor oxygenation states.[28–30] Recently, several different groups including us have uncovered that the therapeutic effect of PDT could be remarkably improved by relieving tumor hypoxia *via* different methods.[31–34] As an opposite strategy, it has been proposed by Bu and Shi that the creation of a tumor hypoxic microenvironment using photosensitizer-doped silica shelled upconversion nanoparticles *via* PDT could be exploited for the activation of intratumorally injected hypoxia-activated prodrug (tirapazamine, TPZ), contributing to a highly effective synergistic cancer therapy.[35] However, the development of biodegradable nanotheranostics with a sequentially activated pattern for PDT-induced, hypoxia-activated chemotherapy delivered *via* systemic administration, remains to be explored to our best knowledge.

In this study, a liposome-based nanotheranostics with the sequential activation pattern is prepared by encapsulating hydrophobic photosensitizer chlorin e6 (*h*Ce6) and hydrophilic AQ4N into the hydrophobic bilayers and aqueous cavity of polyethylene glycol (PEG)

shelled liposomes, respectively (Figure 1). It is demonstrated that the as-prepared AQ4N-*h*Ce6-liposome shows obvious hypoxia-dependent cytotoxicity and effective photodynamic cell killing ability. In addition to its inherent contrasting ability under fluorescence and photo-acoustic imaging, our liposomes may also be used as an imaging probe for positron emission tomography (PET) after chelating $^{64}$Cu isotope. As illustrated by triple-modal imaging, AQ4N-*h*Ce6-liposome is able to gradually accumulate in tumors after intravenous (i.v.) injection. Utilizing the immunofluorescence staining, we uncover that tumors with i.v. injection of AQ4N-*h*Ce6-liposome show obviously increased tumor hypoxia after being irradiated with a 660 nm light-emitting diode (LED) light, favorable for the activation of codelivered AQ4N. As expected, it is uncovered by *in vivo* treatment experiments that mice with i.v. injection of AQ4N-*h*Ce6-liposome followed by 660 nm LED light irradiation show the most effective tumor growth inhibition effect over those control groups. This study demonstrates that our AQ4N-*h*Ce6-liposome is a profound multifunctional nanotheranostics, and such a sequential activation pattern of PDT-triggered, hypoxia-activated chemotherapy is promising for future clinical translation.

## RESULTS AND DISCUSSION

To realize the concept of sequentially activated cancer theranostics, the liposome system was selected as the drug carrier, owing to its efficient loading for both hydrophobic and hydrophilic molecules, high tumor accumulation, and excellent biocompatibility.[36–38] In this work, a commercial hydrophilic AQ4N molecule as the hypoxia-activated prodrug, together with a modified hydrophobic Ce6 (*h*Ce6) as the photosensitizer (by conjugating commercial Ce6 with hexadecylamine, Supporting Figure S1), were simultaneously encapsulated into PEGylated liposomes. In brief, AQ4N-*h*Ce6-lip-osome was prepared by hydrating the dried lipid films formed by mixing 1,2-dipalmitoyl-*sn*-glycero-3-phosphocholine (DPPC), cholesterol, polyethylene glycol-5000 conjugated 1,2-distearoyl-*sn*-glycero-3-phosphoethanolamine (DSPE-mPEG$_{5k}$), and *h*Ce6 at a molar ratio of 6:4:0.5:0.5, with phosphate buffered saline (PBS) containing AQ4N according to the standard method for the preparation of liposomes.[38] As measured by dynamic light scattering (DLS), the as-prepared AQ4N-*h*Ce6-liposome showed uniform size distribution with a mean diameter of ~95 nm (Figure 2a). Under transmittance electron microscopy (TEM), the obtained AQ4N-*h*Ce6-liposome showed uniform sphere-like morphology (Figure 2b). The successful encapsulation of AQ4N and *h*Ce6 into AQ4N-*h*Ce6-liposome was confirmed by their characteristic absorbance peaks at 610 and 404 nm, respectively, on its UV–vis-NIR absorbance spectrum (Figure 2c). The loading efficiencies of AQ4N and *h*Ce6 in those liposomes were determined to be 10.8% and 85%, respectively. Additionally, we uncovered that only ~6% encapsulated AQ4N was released from AQ4N-*h*Ce6-liposome after being incubated in PBS (pH 7.4) for 24 h (Figure S2). Furthermore, it was found that the AQ4N-*h*Ce6-liposome showed efficient singlet oxygen generation ability after exposure to a 660 nm LED light, comparable to that of plain *h*Ce6-liposome (Figure 2d), demonstrating the AQ4N-*h*Ce6-liposome to be an effective nanophotosensitizer.

Next, we evaluated the cellular internalization profiles of the AQ4N-*h*Ce6-liposome, *h*Ce6-liposome, and free AQ4N by using confocal laser scanning microscopy (CLSM). As expected, we found that 4T1 murine breast cancer cells incubated with AQ4N-*h*Ce6-

liposome showed strong fluorescence of both AQ4N and Ce6, while cells incubated with *h*Ce6-liposome or free AQ4N only showed bare Ce6 or AQ4N fluorescence, respectively (Figure 3a). Given that AQ4N would be reduced to AQ4, a potent DNA intercalator/topoisomerase poison, *via* a two-electron process mediated by the CYP3A member of the cytochrome P450 family, the detailed intracellular distribution profile of liposomal AQ4N was studied by utilizing the CLSM.[4] After incubating 4T1 cells with AQ4N-liposome (without adding Ce6 to avoid interference from Ce6 fluorescence) for 12 h under the hypoxic condition, it was found that the red fluorescence was mainly accumulated in the cell nuclei (Figure S3), suggesting the release of AQ4N/AQ4 from cell endosomes/lysosomes. Considering that AQ4N without being reduced would not bind with DNA, it is likely that the fluorescence from cell nuclei may be due to the formation of AQ4 that can effectively bind DNA, though both AQ4N and AQ4 have similar fluorescence emission.[39]

Next, we carefully studied the hypoxia-activated cytotoxicity of both free AQ4N and AQ4N-*h*Ce6-liposome using the standard cell viability assay. It was found that the half-maximal inhibitory concentration ($IC_{50}$) values of AQ4N-*h*Ce6-lip-osome toward 4T1 cells under normoxic and hypoxic condition were 37.8 and 2.0 $\mu$M in terms of AQ4N (Figure 3b), respectively, comparable to those of free AQ4N under the same culture conditions (Figure S4). Those results indicate that AQ4N-*h*Ce6-liposome has a potent and selective cytotoxicity to cells in hypoxia environment. Besides, the photodynamic cytotoxicity of AQ4N-*h*Ce6-liposome was also evaluated with 4T1 cells. We found that cells incubated with AQ4N-*h*Ce6-liposome or *h*Ce6-liposome followed by 660 nm LED light irradiation could be efficiently killed, while those incubated with AQ4N-*h*Ce6-liposome or *h*Ce6-liposome without receiving light irradiation were not obviously disturbed (Figures 3c and S5). Taken together, those results indicate that AQ4N-*h*Ce6-liposome shows effective photodynamic cytotoxicity and hypoxia-activated cytotoxicity, making it promising for PDT-induced, hypoxia-activated cancer therapy.

PET imaging with high spatial resolution and great sensitivity is a power technique for molecular imaging and has been extensively applied for disease diagnosis in the clinic.[40–43] Motivated by the excellent performance of Ce6 in chelating many metal ions (*e.g.*, $Mn^{2+}$, $Gd^{3+}$, $^{64}Cu^{2+}$), we prepared a PET imaging probe by employing the AQ4N-*h*Ce6-liposome as the chelating agent for $^{64}Cu$ isotope ions.[44–47] Consistent with previous reports, our AQ4N-*h*Ce6-liposome showed a high labeling yield for $^{64}Cu^{2+}$, which approached 82.7% after 2 h incubation.[40] Besides, it was found that the as-prepared AQ4N-$^{64}$Cu-*h*Ce6-liposome showed a high labeling stability for $^{64}Cu^{2+}$ after being incubated with mouse serum for 24 h (Figure S6). Moreover, utilizing the cold labeling technique, we found that liposomes after chelation with $Cu^{2+}$ showed no cytotoxicity to cells (Figure S7). Collectively, these results allow the reliable use of AQ4N-$^{64}$Cu-hCe6-liposome as an *in vivo* PET imaging probe.

Next, we used PET imaging to track the AQ4N-$^{64}$Cu-*h*Ce6-liposome after its i.v. injection into Balb/c mice bearing 4T1 tumors (~10 MBq per mouse). Under the microPET Inveon rodent model scanner, it was found that the AQ4N-$^{64}$Cu-*h*Ce6-liposome after i.v. injection could gradually accumulate in tumors (Figure 4a). By quantitatively analyzing the region of interest (ROI) of these PET images, the tumor accumulation of AQ4N-*h*Ce6-liposome was

determined to be 4.9 ± 0.75% ID $g^{-1}$ (percentage injected dose per gram) at 4 h post-injection (p.i.) and kept consistent after 20 h (Figure 4b). Moreover, the tumor-to-muscle (T/M) signal ratio also showed a gradual increase during the first 4 h and kept consistent at ~5 in the following tracking process (Figure S8). In addition, the heart showed high signals even at 24 h p.i., indicating that AQ4N-$^{64}$Cu-*h*Ce6-liposome could have a relatively long blood circulation time.

In order to confirm the accuracy of PET quantification analysis, *ex vivo* distribution analysis was conducted at 24 h p.i. by recording the radioactivity of each organ/tissue using a gamma counter (~10 MBq per mouse). The tumor accumulation of AQ4N-$^{64}$Cu-*h*Ce6-liposome was measured to be 4.7 ± 0.85% ID $g^{-1}$ (Figure 4C), comparable to that evaluated by PET quantification analysis, indicating that PET imaging could be an accurate noninvasive method to evaluate the pharmacokinetic and time-dependent biodistribution profiles of such AQ4N-$^{64}$Cu-*h*Ce6-liposomes. Moreover, similar to many other liposomal drug delivery systems, the AQ4N-$^{64}$Cu-*h*Ce6-liposome had high accumulations in reticuloendothelial systems (RES), including liver and spleen (Figure 4c). However, these RES-retained liposomes should be gradually decomposed into small molecules for excretion with the extension of time.[48,49]

Furthermore, by utilizing the concentration-dependent PA imaging contrasting ability of the AQ4N-*h*Ce6-liposome at 680 nm (Figure S9), the tumor accumulation of those liposomes was studied under the Visualsonic Vevo 2100 LAZER PA imaging system. It was demonstrated that those tumor-bearing mice with i.v. injection of AQ4N-*h*Ce6-liposome showed obviously increased PA signals in tumors, which at 24 h p.i. were about ~2.5 times higher than those without AQ4N-*h*Ce6-liposome injection (Figure 4d,f). Additionally, like previous reports, the strong fluorescence of Ce6 could be employed for *in vivo* tracking of AQ4N-*h*Ce6-liposome under an *in vivo* fluorescence imaging system. We found that AQ4N-*h*Ce6-liposome could efficiently accumulated in tumors after being i.v. injected (Figure 4e,g). All of these results collectively demonstrate that our AQ4N-*h*Ce6-liposome is a versatile probe for *in vivo* tracking under different imaging modalities, all of which uncover that such a AQ4N-*h*Ce6-liposome could efficiently accumulate in tumors *via* passive tumor targeting through the enhanced permeability and retention (EPR) effect.

Next, we evaluate the tumor hypoxia status after PDT by utilizing *ex vivo* immunofluorescence staining with the Pimonidazole as the hypoxia staining probe. A total of 12 mice bearing 4T1 tumors were divided into four groups and received one dose of AQ4N-*h*Ce6-liposome (*h*Ce6 dose: 10 mg $kg^{-1}$) by i.v. injection. At 24 h p.i., one control group of mice was intraperitoneally (i.p.) injected with Pimonidazole (0.6 mg per mouse), a hypoxia marker, and then sacrificed 90 min later. The other three groups of mice were first irradiated with the 660 nm LED light for 1 h (2 mW $cm^{-2}$), received an i.p. injection of Pimonidazole at 5 min, 4 h, or 24 h post-light irradiation, and then sacrificed at 90 min post-Pimonidazole injection. Immunofluorescent staining for Pimonidazole was then carried out to examine the hypoxia status in the tumors. It was found that the tumor slices with photodynamic treatment showed obviously increased tumor hypoxia compared to those without photodynamic treatment (Figure 5a). By semi-quantitative analysis of hypoxia-positive signals in those tumor slices, we uncovered that the percentages of hypoxia positive

area dramatically increased from ~34% for those without photodynamic treatment to ~51%, ~61%, and ~58% for those collected at 5 min, 4 h, and 24 h post-photodynamic treatment with AQ4N-*h*Ce6-liposome, respectively (Figure 5b).

To uncover the reasons leading to such significantly increased tumor hypoxia except for the fast oxygen depletion during the photodynamic treatment process,[50–52] we carefully examined the status of the tumor blood vasculatures post-photodynamic treatment. By utilizing the immunofluorescence staining, it was found that blood vessels in those tumor slices collected at 4 h post-photodynamic treatment with AQ4N-*h*Ce6-liposome (*h*Ce6 dose: 10 mg $kg^{-1}$; light dose: 660 nm, 2 mW $cm^{-2}$, 1 h) were severely damaged and became compressed in comparison with those without light exposure (Figure 5c). By semiquantitatively analyzing the area of those opened blood vessels, which were considered as effective blood vessels, we found that the percentage of effective blood vessel area remarkably dropped from ~3.9% in those slices without photodynamic treatment to ~1.2% for those collected at 4 h post-photodynamic treatment (Figure 5d). Such severely damaged tumor blood vessels would remarkably impede the tumor oxygen supply, collectively contributing to significantly aggravated tumor hypoxia with the fast oxygen depletion during photodynamic treatment.

The strong tumor hypoxia is expected to be favorable for the activation of AQ4N to a toxic chemo-drug. Next, the light-triggered therapeutic effect of AQ4N-*h*Ce6-liposome was evaluated on 4T1 tumor bearing mice. A total of 30 female Balb/c mice bearing 4T1 tumors with sizes of ~100 $mm^3$ were randomly divided into 5 groups ($n$ = 6 per group) as follows: (I) control group by saline injection only; (II) bare PDT group by plain *h*Ce6-liposome injection plus 660 nm LED light exposure; (III) plain *h*Ce6-liposome and free AQ4N injection plus light exposure; (IV) AQ4N-*h*Ce6-liposome injection only without light exposure; and (V) AQ4N-*h*Ce6-liposome injection plus light exposure. In our experiments, light irradiation was carried out by exposing mice to 660 nm LED light exposure at the power density of 2 mW $cm^{-2}$ for 1 h at 24 h post-injection of various agents. The *h*Ce6 and AQ4N doses were 10 and 5 mg $kg^{-1}$ in related groups, respectively. Then, the tumor sizes were measured using a digital caliper for 14 days after the beginning of treatment. Tumors collected from each treated group of mice were weighed 14 days post-treatment. Compared to tumors on mice treated by plain *h*Ce6-liposome injection plus 660 nm LED light exposure or AQ4N-*h*Ce6-liposome injection only, the tumor growth of those mice that received i.v. injection of AQ4N-*h*Ce6-liposome plus light irradiation was the most effectively regressed (Figure 6a,b). Our results indicate that such a PDT-induced, hypoxia-activated therapy with the AQ4N-*h*Ce6-liposome is an effective strategy in inhibiting tumor growth. Moreover, it was observed that the tumor growth inhibition effect on the mice treated by plain *h*Ce6-liposome and free AQ4N injection plus light exposure (group III) was less effective in comparison with the group V with AQ4N-*h*Ce6-liposome plus light, likely owing to the fast excretion and less effcient tumor accumulation of AQ4N in its free form.

To further confirm the therapeutic effect, the histological changes and apoptosis levels of tumors were analyzed in detail by utilizing both hematoxylin and eosin (H&E) staining and terminal deoxynucleotidyl transferase dUTP nick end labeling (TUNEL) assay, respectively, at 24 h post various treatments. Based on H&E staining, severe morphology change and

necrosis were observed for tumors treated with AQ4N-*h*Ce6-liposome injection plus 660 nm LED light irradiation, while only moderate levels of damages were observed for tumors of the other three controls groups of mice treated with bare PDT or AQ4N-*h*Ce6-liposome without light-activation (Figure 6c). Moreover, the apoptosis levels in tumors revealed by TUNEL assay followed the same trend (Figure 6d). Taken together, those results demonstrate that such sequentially activated tumor therapy with AQ4N-*h*Ce6-liposome is a promising strategy for efficient cancer treatment. *Via* this approach, the first applied PDT would not only kill cancer cells with sufficient oxygen supplying but also generate a highly hypoxic tumor microenvironment by consuming oxygen inside the solid tumors and inducing severe tumor blood vasculature damage (Figure 5c,d) to delay tumor reoxygenation, so as to allow further activation of AQ4N to kill the remaining tumor cells.

## CONCLUSION

In this study, we designed a multifunctional theranostic liposome and confirmed it to be a promising agent for cancer treatment *via* PDT-induced, hypoxia-activated therapy. By utilizing the strong absorbance, fluorescence, and $^{64}Cu^{2+}$ chelating ability of Ce6, the as-prepared AQ4N-*h*Ce6-liposome was demonstrated to be a versatile imaging probe for *in vivo* tracking *via* PA imaging, fluorescence imaging, and PET imaging, respectively. *Ex vivo* immunofluorescence staining uncovered that PDT post-i.v. injection of the AQ4N-*h*Ce6-liposome could induce severe tumor hypoxia, favorable for the activation of AQ4N also delivered into tumors by these liposomes, contributing to the effective cancer treatment outcomes. Collectively, such a AQ4N-*h*Ce6-liposome shows several advantages as a multifunctional cancer theranostic: (1) its sequential activation pattern could contribute to a promising synergistic cancer treatment strategy by taking advantage of the PDT-induced tumor hypoxia, a severe limiting factor of conventional PDT; (2) its versatility as an imagable probe would facilitate tumor imaging and real-time *in vivo* monitoring of this theranostic agent, so as to enable better treatment planning; and (3) its excellent biocompatibility and well-defined composition would make it a promising candidate for future clinical translation.

## MATERIALS AND EXPERIMENTS

### Materials

Ce6 was purchased from Frontier Scientific, Inc. DPPC was purchased from Xi'an Ruixi Biological Technology Co., Ltd. DSPE-mPEG$_{5k}$ was purchased from Laysan Bio Inc. AQ4N was purchased from Abcam. Hexadecylamine, *N*-(3-(dimethylamino)-propyl)-*N*-ethylcarbodiimide hydrochloride crystalline (EDC), *N*-hydroxysuccinimide (NHS), and 3-(4,5-dimethylthiazol-2-yl)-2,5-diphenyl-tetrazolium bromide (MTT) were all purchased from Sigma-Aldrich. RPMI-1640 medium and fetal bovine serum (FBS) were purchased from Thermo Fisher Scientific Inc. All other chemicals were purchased from China National Pharmaceutical Group Corporation.

### Synthesis of Hexadecylamine Conjugated Ce6 (*h*Ce6)

Hexadecylamine conjugated Ce6 was prepared by conjugating commercial Ce6 with hexylamine in the presence of EDC and NHS. Briefly, Ce6 (100 mg, 0.17 mmol), hexadecylamine (164 mg, 0.68 mmol), EDC (132 mg, 0.68 mmol), NHS (77 mg, 0.68 mmol), and trimethylamine (TEA, 95 μL, 0.68 mmol) were dissolved in 10 mL anhydrous dichloromethane and stirred at room temperature for 24 h. Afterward, the reaction mixture was condensed by rotary evaporation and then purified by thin layer chromatography (TLC) using a mixture of dichloromethane/ethyl acetate (1:2, v/v) as the solvent system (RF, 0.7). Afterward, the individual band was scraped, dispersed with methanol, and centrifuged to collect the supernatant. The successful synthesis of *h*Ce6 was confirmed by the matrix-assisted laser desorption/ionization time-of-flight mass spectrometry (MALDI-TOF MS). MALDI-TOF *m*/*z* calculated for $C_{82}H_{135}N_7O_3$ $[M + Na]^+$ 1289.06, found 1289.39.

### Liposome Preparation

To prepare AQ4N-*h*Ce6-liposome, the lipid mixture of DPPC, cholesterol, DSPE-mPEG5k, and *h*Ce6 at a molar ratio of 6:4:0.5:0.5 was dissolved in chloroform and then dried under a rotary evaporator. Afterward, the dried lipid film was hydrated with a AQ4N solution (10 mg $mL^{-1}$) and stirred at 45 °C for 30 min, followed by being extruded through a 200 nm polycarbonate filter at 45 °C for 20 times. The unencapsulated AQ4N was removed *via* a sephadex G-50 column. The obtained AQ4N-*h*Ce6-liposome was condensed with an Amico filter device with a molecule weight cutoff (MWCO) of 100 kDa (Millipore, Bedford, MA) for further use. Plain *h*Ce6-lipsome was prepared following the same procedure used for the preparation of AQ4N-*h*Ce6-liposome just without the addition of AQ4N.

The morphology of liposomes after being stained by phosphotungstic acid (1 wt %) was observed under TEM (Tecnai F20, FEI). The size distribution, absorbance, and fluorescence spectra of AQ4N-*h*Ce6-liposome and Ce6-liposome were recorded using a Malvern zetasizer (nano-ZS90), a UV–vis-NIR spectrometer (Thermo Fisher), and a FluoroMax 4 luminescence spectrometer (HORIBA Jobin Yvon), respectively. The concentrations of AQ4N and *h*Ce6 were quantified using their absorbance at 610 and 404 nm with mass extinction coefficient of 22.5 mL $mg^{-1}$ $cm^{-1}$ and 161 mL $mg^{-1}$ $cm^{-1}$, respectively.

### Evaluation of the Singlet Oxygen Generation Ability of AQ4N-*h*Ce6-Liposome

The solutions of AQ4N-*h*Ce6-liposome and plain *h*Ce6-liposome at an *h*Ce6 concentration of 5 μM in phosphate buffered solution (PBS) were mixed with a commercial singlet oxygen sensor green (SOSG) probe at a final concentration of 2.5 μM and then subjected to a 660 nm LED light at 2 mW $cm^{-2}$. At 5, 10, and 20 min post-irradiation, 100 μL sample was pipetted out from each well, and the fluorescence intensity of SOSG was recorded using a multimode microreader (Varioskan Flash, Thermo Fisher).

### Cellular Uptake of AQ4N-*h*Ce6-Liposome and Its Intra-cellular Distribution

The 4T1 murine breast cancer cells were ordered from American Type Culture Collection (ATCC) and maintained according to the recommended procedure. For confocal laser scanning microscopy (CLSM) observation, the 4T1 cells were seeded in a 24-well plate containing circle glass coverslides at a density of $3 \times 10^4$ cells per well. After being

incubated at 37 °C for 24 h, the cells were cultured with fresh medium containing AQ4N-*h*Ce6-liposome, plain *h*Ce6-liposome, and free AQ4N (incubation concentration: *h*Ce6 = 20 μM, AQ4N = 10 μM) for another 4 h. After that, the cells were washed twice with PBS, fixed with 4% paraformalclehyde solution, stained with 4,6-diamino-2-phenyl indole (DAPI), and finally observed under the CLSM (Leica TCS-SP5II, Germany).

To study the intracellular distribution and metabolic profile of AQ4N under hypoxia, AQ4N-liposome was prepared according to the same procedure for AQ4N-*h*Ce6-liposome just without addition of *h*Ce6 and utilized as a model liposomal AQ4N to avoid the disturbance of Ce6 fluorescence under CLSM imaging. Briefly, 4T1 cells were seeded in a 24-well plate containing circle glass coverslides at a density of $5 \times 10^4$ cells per well and incubated under a normaxic condition (95% air, 5% $CO_2$) for 24 h. After that, the cells were cultured with fresh medium containing AQ4N-liposome (AQ4N = 10 μM) under a hypoxic condition (1% $O_2$, 5% $CO_2$ balanced with $N_2$) for 12 h. After removal of AQ4N-liposome containing medium, the cells was recultured with the fresh medium containing Lyso-tracker red at a concentration of 100 nM for additional 1 h at 37 °C. Then, the cells were washed twice with PBS, fixed with 4% paraformalclehyde solution, stained with 4,6-diamino-2-phenyl indole (DAPI), and finally observed under the CLSM.

### Cytotoxicity of AQ4N-*h*Ce6-Liposome in Hypoxia

The 4T1 cells were seeded in 96-well plate at a density of $2 \times 10^3$ cells per well and incubated in normoxic condition for 24 h. Then, the cells were incubated with AQ4N-hCe6-liposome or free AQ4N at a series of concentrations in normoxic or hypoxic condition for another 24 h. After removal of drug-containing medium, the cells were recultured in fresh medium in normoxic condition for additional 48 h. After being incubated with MTT at a concentration of 1 mg $mL^{-1}$ for 4 h, the medium was discarded, and formazan was dissolved by adding 150 μL DMSO. Then the absorbance of each well at 570 nm was recorded using a microreader (Model 680, Bio-Rad) to determine the relative cell viabilities.

### *In Vitro* Photodynamic Toxicity of AQ4N-*h*Ce6-Liposome and *h*Ce6-Liposome

The 4T1 cells were seeded in 96-well plate at a density of $1 \times 10^4$ cells per well and incubated in normoxic condition for 24 h. After being incubated with AQ4N-*h*Ce6-liposome or plain *h*Ce6-liposome for 4 h, the cells were removed from liposome containing medium and irradiated with a 660 nm LED light for 30 min. At 20 h post-laser irradiation, the cells were incubated with MTT solution to evaluate their photodynamic toxicity according to same procedure as aforementioned.

### Tumor Models

Female Balb/c mice mice of 18–20 g were purchased from Nanjing Sikerui Biological Technology Co. Ltd. and used under protocols approved by the laboratory animal center of Soochow University. To build the 4T1 tumor model, $2 \times 10^6$ 4T1 cells in 50 μL PBS were subcutaneously injected to the back of each mouse. The mice were used when the tumor volumes reached ~100 $mm^3$.

### $^{64}$Cu Labeling and PET Imaging

The $^{64}$Cu was produced with an onsite cyclotron (GE PETtrace). Briefly, $^{64}CuCl_2$ (~150 MBq) was diluted in 300 μL of 0.1 M sodium acetate buffer (pH 5.5) and mixed with 100 μL of AQ4N-*h*Ce6-liposome (0.2 mg/mL in terms of Ce6). After being incubated at 37 °C for 60 min under constant shaking, excess $^{64}CuCl_2$ was removed using a Sephadex G-25 column with PBS as the mobile phase. The labeling yield was determined by TLC at different time points.

The serum stability study was carried out to ensure the $^{64}$Cu isotope was stably attached into AQ4N-*h*Ce6-liposome. Briefly, $^{64}$Cu-labeled AQ4N-*h*Ce6-liposome was incubated in PBS or serum at 37 °C for up to 24 h. At different time intervals, a portion of the mixture was sampled and filtered through an Amico filter device with a MWCO of 300 kDa. The retained (*i.e.*, intact) radioactivity of $^{64}$Cu on AQ4N-*h*Ce6-liposome was recorded with a gamma-counter (PerkinElmer, USA). The serum stability was calculated using the following equation: radioactivity on filter/total sampled radioactivity) × 100%.

For PET imaging, 4T1 tumor-bearing mice (3 mice per group) received i.v. injection of the $^{64}$Cu-labeled AQ4N-*h*Ce6-liposome at a dose of ~10 MBq and were imaged using a microPET/microCT Inveon rodent model scanner (Siemens Medical Solutions USA, Inc.) at different time intervals. Data acquisition, image reconstruction, and ROI analysis of the PET data were performed according to previously developed methods.[40,42] At 24 h p.i., *ex vivo* biodistribution study was carried out to determine the % ID/g values of each organ using PET imaging. Briefly, mice were euthanized, and with their blood, tumor, and major organs/tissues were collected, wet-weighed, and recorded using a gamma-counter. Data are presented as %ID/g (mean ± SD).

### *In Vivo* PA and Fluorescence Imaging

For PA imaging, the 4T1 tumor-bearing mice were anesthetized and then injected with AQ4N-*h*Ce6-liposomes at a dose of 5 mg kg$^{-1}$ (in terms of *h*Ce6). Then, at different time intervals p.i., the tumor region was imaged using the Visualsonic Vevo 2100 LAZER system with an excitation wavelength at 680 nm.

For fluorescence imaging, tumor-bearing mice were anesthetized and injected with AQ4N-*h*Ce6-liposome at dose of 5 mg kg$^{-1}$ (in terms of *h*Ce6). Then, at different time intervals p.i., the mice were imaged under a Maestro *in vivo* optical imaging system (Cambridge Research & Instrumentation, Inc.) with excitation at 661 nm.

### Photodynamic Treatment Induced Tumor Microenvironment Change

*Ex vivo* immunofluorescence staining was utilized to evaluate the photodynamic treatment induced tumor hypoxia evolution. Briefly, the 4T1 tumor-bearing mice with i.v. injection of AQ4N-*h*Ce6-liposomes (*h*Ce6 dose = 10 mg kg$^{-1}$) were irradiated with a 660 nm LED light for 1 h at 24 h p.i. Then, mice without LED light irradiation and those with light exposure at 5 min, 4 h, or 24 h post-irradiation were intraperitoneally injected with Pimonidazole hydrochloride (Hypoxyprobe, USA) at a dose of 30 mg kg$^{-1}$ according to the procedure provided by the manufacturer. The mice were sacrificed 90 min later to collect frozen tumor

slices, which were first stained with a mixture of mouse antipimonidazole monoclonal antibody and ratantimouse CD31 antibody as primary antibodies to label tumor hypoxia regions and blood vessels, respectively. Afterward, the slices were then stained with Alexa Fluo 488 conjugated goat-antimouse antibody and rhodamine conjugated donkey-antirat antibody as secondary antibodies. Finally, the slices were imaged using CLSM. The hypoxia region and the density of blood vessels of each slice were statistically analyzed using the Imaging-J software according to the previously used procedures.

To explore the effect of photodynamic treatment on the morphology of blood vessels, the 4T1 tumor-bearing mice received an i.v. injection of AQ4N-*h*Ce6-liposomes at a dose of (*h*Ce6 dose = 10 mg $kg^{-1}$) and were exposed to 660 nm LED light for 24 h p.i. At 4 h post-irradiation, the mice were sacrificed to collect frozen tumor slices, which were first stained with ratantimouse CD31 antibody and then Alexa Fluo 488 conjugated donkey-antirat antibody. Finally, the slices were imaged using the CLSM.

### *In Vivo* Combination Cancer Therapy with AQ4N-*h*Ce6-Liposome

Thirty female Balb/c mice bearing 4T1 tumors were randomly divided to 5 groups. When the tumor sizes reached ~100 $mm^3$, three groups of those mice were i.v. injected with saline, plain *h*Ce6-liposome, or a mixture of free AQ4N and plain *h*Ce6-liposome. The other two groups of those mice were i.v. injected with AQ4N-*h*Ce6-liposome. The doses of Ce6 and AQ4N were 10 and 5 mg $kg^{-1}$, respectively. At 24 h p.i., one group of mice with i.v. injection of AQ4N-*h*Ce6-liposome and another two groups of mice with i.v. injection of plain *h*Ce6-liposome and a mixture of free AQ4N and *h*Ce6-liposome were irradiated with a 660 nm LED light for 1 h at a power density of 2 mW $cm^{-2}$. Since the beginning of the treatment, the tumor length and width of each mouse were recorded using a digital caliper every 2 days. The tumor volume ($V$) was calculated by the following equation: $V = LW^2/2$, in which $L$ and $W$ refer to the length and width of the tumor in millimeters, respectively. In addition, the body weight of each mouse was also measured using a digital balance every the other day. At day 14 post-treatment, the mice were sacrificed, and their tumors were collected for weighing. Moreover, the main organs including liver, spleen, kidney, heart, and lung of saline injected control group and AQ4N-*h*Ce6-liposome injected combination therapy group were collected, fixed using 4% paraformalclehyde solution, mounted with parafine, sliced, stained with H&E, and then imaged using a microscopy. To evaluate the therapeutic effects of those different treatments, one mouse from each group was sacrificed 1 day post-laser irradiation, with its tumor collected and splitted into two halves for H&E and TUNEL staining, respectively.

## Supplementary Material

Refer to Web version on PubMed Central for supplementary material.

## Acknowledgments

This work was partially supported by the National Research Programs from Ministry of Science and Technology (MOST) of China (2016YFA0201200), the National Natural Science Foundation of China (51525203), a Juangsu Natural Science Fund for Distinguished Young Scholars (BK20130005), Collaborative Innovation Center of Suzhou Nano Science and Technology, a Project Funded by the Priority Academic Program Development (PAPD) of

Jiangsu Higher Education Institutions, the Macao Science and Technology Development Fund (096/2015/A3), the Research Fund of the University of Macau (MYRG2014-00033-ICMS-QRCM, MYRG2014-00051-ICMS-QRCM), the National Institutes of Health (NIBIB/NCI 1R01CA169365 and P30CA014520), and the American Cancer Society (125246-RSG-13-099-01-CCE).

## References

1. Semenza GL. The Hypoxic Tumor Microenvironment: A Driving Force for Breast Cancer Progression. Biochim Biophys Acta, Mol Cell Res. 2016; 1863:382–391.
2. Brown JM, Giaccia AJ. The Unique Physiology of Solid Tumors: Opportunities (and Problems) for Cancer Therapy. Cancer Res. 1998; 58:1408–1416. [PubMed: 9537241]
3. Swartz MA, Iida N, Roberts EW, Sangaletti S, Wong MH, Yull FE, Coussens LM, DeClerck YA. Tumor Microenvironment Complexity: Emerging Roles in Cancer Therapy. Cancer Res. 2012; 72:2473–2480. [PubMed: 22414581]
4. Brown JM, Wilson WR. Exploiting Tumour Hypoxia in Cancer Treatment. Nat Rev Cancer. 2004; 4:437–447. [PubMed: 15170446]
5. Wilson WR, Hay MP. Targeting Hypoxia in Cancer Therapy. Nat Rev Cancer. 2011; 11:393–410. [PubMed: 21606941]
6. Harris AL. Hypoxia: A Key Regulatory Factor in Tumour Growth. Nat Rev Cancer. 2002; 2:38–47. [PubMed: 11902584]
7. Patel A, Sant S. Hypoxic Tumor Microenvironment: Opportunities to Develop Targeted Therapies. Biotechnol Adv. 2016; 34:803–812. [PubMed: 27143654]
8. Huang CC, Chia WT, Chung MF, Lin KJ, Hsiao CW, Jin C, Lim WH, Chen CC, Sung HW. An Implantable Depot That Can Generate Oxygen *in Situ* for Overcoming Hypoxia-Induced Resistance to Anticancer Drugs in Chemotherapy. J Am Chem Soc. 2016; 138:5222–5225. [PubMed: 27075956]
9. Kumar R, Kim EJ, Han J, Lee H, Shin WS, Kim HM, Bhuniya S, Kim JS, Hong KS. Hypoxia-Directed and Activated Theranostic Agent: Imaging and Treatment of Solid Tumor. Biomaterials. 2016; 104:119–128. [PubMed: 27449948]
10. Song X, Feng L, Liang C, Gao M, Song G, Liu Z. Liposomes Co-Loaded with Metformin and Chlorin e6 Modulate Tumor Hypoxia during Enhanced Photodynamic Therapy. Nano Res. 2016; doi: 10.1007/s12274-016-1274-8
11. Fan W, Bu W, Shi J. On The Latest Three-Stage Development of Nanomedicines Based on Upconversion Nanoparticles. Adv Mater. 2016; 28:3987–4011. [PubMed: 27031300]
12. Denny WA. The Role of Hypoxia-Activated Prodrugs in Cancer Therapy. Lancet Oncol. 2000; 1:25–29. [PubMed: 11905684]
13. Weiss GJ, Infante JR, Chiorean EG, Borad MJ, Bendell JC, Molina JR, Tibes R, Ramanathan RK, Lewandowski K, Jones SF, Lacouture ME, Langmuir VK, Lee H, Kroll S, Burris HA. Phase 1 Study of the Safety, Tolerability, and Pharmacokinetics of TH-302, A Hypoxia-Activated Prodrug, in Patients with Advanced Solid Malignancies. Clin Cancer Res. 2011; 17:2997–3004. [PubMed: 21415214]
14. Denny WA. Hypoxia-Activated Prodrugs in Cancer Therapy: Progress to the Clinic. Future Oncol. 2010; 6:419–428. [PubMed: 20222798]
15. Ganjoo KN, Cranmer LD, Butrynski JE, Rushing D, Adkins D, Okuno SH, Lorente G, Kroll S, Langmuir VK, Chawla SP. A Phase I Study of the Safety and Pharmacokinetics of the Hypoxia-Activated Prodrug TH-302 in Combination with Doxorubicin in Patients with Advanced Soft Tissue Sarcoma. Oncology. 2011; 80:50–56. [PubMed: 21625179]
16. Chawla SP, Cranmer LD, Van Tine BA, Reed DR, Okuno SH, Butrynski JE, Adkins DR, Hendifar AE, Kroll S, Ganjoo KN. Phase II Study of the Safety and Antitumor Activity of the Hypoxia-Activated Prodrug TH-302 in Combination with Doxorubicin in Patients with Advanced Soft Tissue Sarcoma. J Clin Oncol. 2014; 32:3299–3306. [PubMed: 25185097]
17. Borad MJ, Reddy SG, Bahary N, Uronis HE, Sigal D, Cohn AL, Schelman WR, Stephenson J, Chiorean EG, Rosen PJ, Ulrich B, Dragovich T, Del Prete SA, Rarick M, Eng C, Kroll S, Ryan DP. Randomized Phase II Trial of Gemcitabine Plus TH-302 *Versus* Gemcitabine in Patients With Advanced Pancreatic Cancer. J Clin Oncol. 2015; 33:1475–1481. [PubMed: 25512461]

18. Williams KJ, Albertella MR, Fitzpatrick B, Loadman PM, Shnyder SD, Chinje EC, Telfer BA, Dunk CR, Harris PA, Stratford IJ. *In vivo* Activation of the Hypoxia-Targeted Cytotoxin AQ4N in Human Tumor Xenografts. Mol Cancer Ther. 2009; 8:3266–3275. [PubMed: 19996276]
19. Yuan Y, Zhang CJ, Kwok RTK, Xu S, Zhang R, Wu J, Tang BZ, Liu B. Light-Up Probe for Targeted and Activatable Photodynamic Therapy with Real-Time *In Situ* Reporting of Sensitizer Activation and Therapeutic Responses. Adv Funct Mater. 2015; 25:6586–6595.
20. Dougherty TJ, Gomer CJ, Henderson BW, Jori G, Kessel D, Korbelik M, Moan J, Peng Q. Photodynamic Therapy. J Natl Cancer Inst. 1998; 90:889–905. [PubMed: 9637138]
21. Dolmans DEJGJ, Fukumura D, Jain RK. Photodynamic Therapy for Cancer. Nat Rev Cancer. 2003; 3:380–387. [PubMed: 12724736]
22. Cheng L, Wang C, Feng L, Yang K, Liu Z. Functional Nanomaterials for Phototherapies of Cancer. Chem Rev. 2014; 114:10869–10939. [PubMed: 25260098]
23. Feng B, Zhou F, Wang D, Xu Z, Yu H, Li Y. Gold Nanomaterials for Treatment of Metastatic Cancer. Sci China: Chem. 2016; 59:984.
24. Yuan Y, Feng G, Qin W, Tang BZ, Liu B. Targeted and Image-Guided Photodynamic Cancer Therapy Based on Organic Nanoparticles with Aggregation-Induced Emission Characteristics. Chem Commun. 2014; 50:8757–8760.
25. Wang D, Wang T, Liu J, Yu H, Jiao S, Feng B, Zhou F, Fu Y, Yin Q, Zhang P, Zhang Z, Zhou Z, Li Y. Acid-Activatable Versatile Micelleplexes for PD-L1 Blockade-Enhanced Cancer Photo-dynamic Immunotherapy. Nano Lett. 2016; 16:5503–5513. [PubMed: 27525587]
26. Ai X, Ho CJH, Aw J, Attia ABE, Mu J, Wang Y, Wang X, Wang Y, Liu X, Chen H, Gao M, Chen X, Yeow EKL, Liu G, Olivo M, Xing B. *In vivo* Covalent Cross-Linking of Photon-Converted Rare-Earth Nanostructures for Tumour Localization and Theranostics. Nat Commun. 2016; 7:10432–10440. [PubMed: 26786559]
27. Ai X, Mu J, Xing B. Recent Advances of Light-Mediated Theranostics. Theranostics. 2016; 6:2439–2457. [PubMed: 27877246]
28. Foster TH, Murant RS, Bryant RG, Knox RS, Gibson SL, Hilf R. Oxygen Consumption and Diffusion Effects in Photodynamic Therapy. Radiat Res. 1991; 126:296–303. [PubMed: 2034787]
29. Foster TH, Gao L. Dosimetry in Photodynamic Therapy: Oxygen and the Critical Importance of Capillary Density. Radiat Res. 1992; 130:379–383. [PubMed: 1594766]
30. Song X, Chen Q, Liu Z. Recent Advances in the Development of Organic Photothermal Nano-Agents. Nano Res. 2015; 8:340–354.
31. Song X, Feng L, Liang C, Yang K, Liu Z. Ultrasound Triggered Tumor Oxygenation with Oxygen-Shuttle Nanoperfluorocarbon to Overcome Hypoxia-Associated Resistance in Cancer Therapies. Nano Lett. 2016; 16:6145–6153. [PubMed: 27622835]
32. Cheng Y, Cheng H, Jiang C, Qiu X, Wang K, Huan W, Yuan A, Wu J, Hu Y. Perfluorocarbon Nanoparticles Enhance Reactive Oxygen Levels and Tumour Growth Inhibition in Photodynamic Therapy. Nat Commun. 2015; 6:8785–8792. [PubMed: 26525216]
33. Chen Q, Feng L, Liu J, Zhu W, Dong Z, Wu Y, Liu Z. Intelligent Albumin-MnO2 Nanoparticles as pH-/$H_2O_2$-Responsive Dissociable Nanocarriers to Modulate Tumor Hypoxia for Effective Combination Therapy. Adv Mater. 2016; 28:7129–7136. [PubMed: 27283434]
34. Song G, Chen Y, Liang C, Yi X, Liu J, Sun X, Shen S, Yang K, Liu Z. Catalase-Loaded TaOx Nanoshells as Bio-Nanoreactors Combining High-Z Element and Enzyme Delivery for Enhancing Radiotherapy. Adv Mater. 2016; 28:7143–7148. [PubMed: 27275921]
35. Liu Y, Liu Y, Bu W, Cheng C, Zuo C, Xiao Q, Sun Y, Ni D, Zhang C, Liu J, Shi J. Hypoxia Induced by Upconversion-Based Photodynamic Therapy: Towards Highly Effective Synergistic Bioreductive Therapy in Tumors. Angew Chem. 2015; 127:8223–8227.
36. Luo D, Carter KA, Razi A, Geng J, Shao S, Lin C, Ortega J, Lovell JF. Porphyrin-Phospholipid Liposomes with Tunable Leakiness. J Controlled Release. 2015; 220:484–494.
37. Luo D, Li N, Carter KA, Lin C, Geng J, Shao S, Huang WC, Qin Y, Atilla-Gokcumen GE, Lovell JF. Rapid Light-Triggered Drug Release in Liposomes Containing Small Amounts of Unsaturated and Porphyrin-Phospholipids. Small. 2016; 12:3039–3047. [PubMed: 27121003]

38. Feng L, Gao M, Tao D, Chen Q, Wang H, Dong Z, Chen M, Liu Z. Cisplatin-Prodrug-Constructed Liposomes as A Versatile Theranostic Nanoplatform for Bimodal Imaging Guided Combination Cancer Therapy. Adv Funct Mater. 2016; 26:2207–2217.
39. Patterson LH, McKeown SR. AQ4N: A New Approach to Hypoxia-Activated Cancer Chemotherapy. Br J Cancer. 2000; 83:1589–1593. [PubMed: 11104551]
40. Cheng L, Kamkaew A, Sun H, Jiang D, Valdovinos HF, Gong H, England CG, Goel S, Barnhart TE, Cai W. Dual-Modality Positron Emission Tomography/Optical Image-Guided Photodynamic Cancer Therapy with Chlorin e6-Containing Nano-micelles. ACS Nano. 2016; 10:7721–7730. [PubMed: 27459277]
41. Liu T, Shi S, Liang C, Shen S, Cheng L, Wang C, Song X, Goel S, Barnhart TE, Cai W, Liu Z. Iron Oxide Decorated MoS2 Nanosheets with Double PEGylation for Chelator-Free Radiolabeling and Multimodal Imaging Guided Photothermal Therapy. ACS Nano. 2015; 9:950–960. [PubMed: 25562533]
42. Cheng L, Shen S, Shi S, Yi Y, Wang X, Song G, Yang K, Liu G, Barnhart TE, Cai W, Liu Z. FeSe2-Decorated $Bi_2Se_3$ Nanosheets Fabricated *via* Cation Exchange for Chelator-Free $^{64}$Cu-Labeling and Multimodal Image-Guided Photothermal-Radiation Therapy. Adv Funct Mater. 2016; 26:2185–2197. [PubMed: 27110230]
43. Liu Z, Cai W, He L, Nakayama N, Chen K, Sun X, Chen X, Dai H. *In vivo* Biodistribution and Highly Efficient Tumour Targeting of Carbon Nanotubes in Mice. Nat Nanotechnol. 2007; 2:47–52. [PubMed: 18654207]
44. Keca JM, Chen J, Overchuk M, Muhanna N, MacLaughlin CM, Jin CS, Foltz WD, Irish JC, Zheng G. Nanotexaphyrin: One-Pot Synthesis of A Manganese Texaphyrin-Phospholipid Nanoparticle for Magnetic Resonance Imaging. Angew Chem. 2016; 128:6295–6299.
45. Gong H, Dong Z, Liu Y, Yin S, Cheng L, Xi W, Xiang J, Liu K, Li Y, Liu Z. Engineering of Multifunctional Nano-Micelles for Combined Photothermal and Photodynamic Therapy Under the Guidance of Multimodal Imaging. Adv Funct Mater. 2014; 24:6492–6502.
46. MacDonald TD, Liu TW, Zheng G. An MRI-Sensitive, Non-Photobleachable Porphysome Photothermal Agent. Angew Chem, Int Ed. 2014; 53:6956–6959.
47. Liu TW, MacDonald TD, Shi J, Wilson BC, Zheng G. Intrinsically Copper-64-Labeled Organic Nanoparticles as Radio-tracers. Angew Chem, Int Ed. 2012; 51:13128–13131.
48. Phan G, Herbet A, Cholet S, Benech H, Deverre JR, Fattal E. Pharmacokinetics of DTPA Entrapped in Conventional and Long-Circulating Liposomes of Different Size for Plutonium Decorporation. J Controlled Release. 2005; 110:177–188.
49. Paoli EE, Kruse DE, Seo JW, Zhang H, Kheirolomoom A, Watson KD, Chiu P, Stahlberg H, Ferrara KW. An Aptical and MicroPET Assessment of Thermally-Sensitive Liposome Bio-distribution in the Met-1 Tumor Model: Importance of Formulation. J Controlled Release. 2010; 143:13–22.
50. Sitnik TM, Hampton JA, Henderson BW. Reduction of Tumour Oxygenation during and after Photodynamic Therapy *in vivo*: Effects of Fluence Rate. Br J Cancer. 1998; 77:1386–1394. [PubMed: 9652753]
51. Jo J, Lee CH, Kopelman R, Wang X. In Lifetime-Resolved Photoacoustic (LPA) Spectroscopy for Monitoring Oxygen Change and Photodynamic Therapy (PDT). Proc SPIE. 2016:97081L.
52. Henderson BW, Busch TM, Vaughan LA, Frawley NP, Babich D, Sosa TA, Zollo JD, Dee AS, Cooper MT, Bellnier DA, Greco WR, Oseroff AR. Photofrin Photodynamic Therapy Can Significantly Deplete or Preserve Oxygenation in Human Basal Cell Carcinomas during Treatment, Depending on Fluence Rate. Cancer Res. 2000; 60:525–529. [PubMed: 10676629]

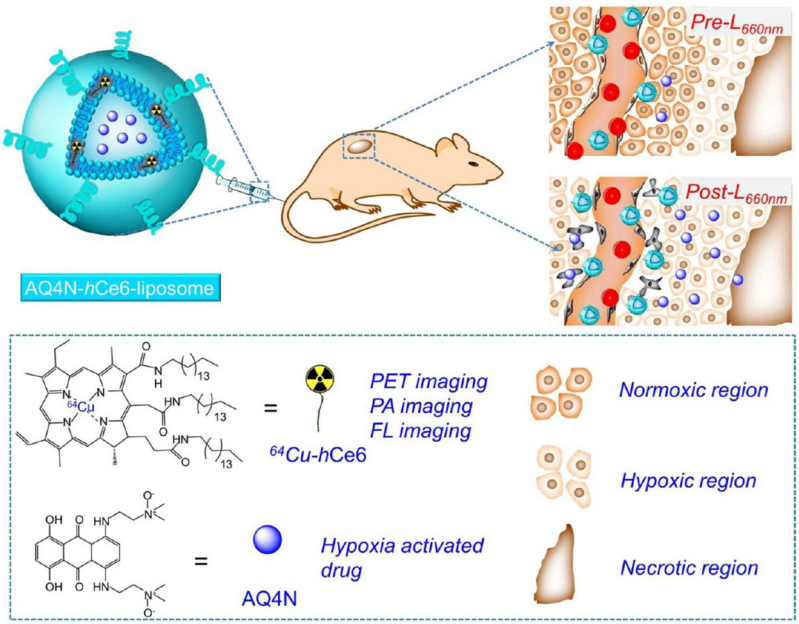


**Figure 1.**

A scheme illustrating the chemical composition of AQ4N-*h*Ce6-liposome, which can serve as a multifunctional theranostic agent for multimodal imaging and PDT-induced, hypoxia-activated cancer therapy.

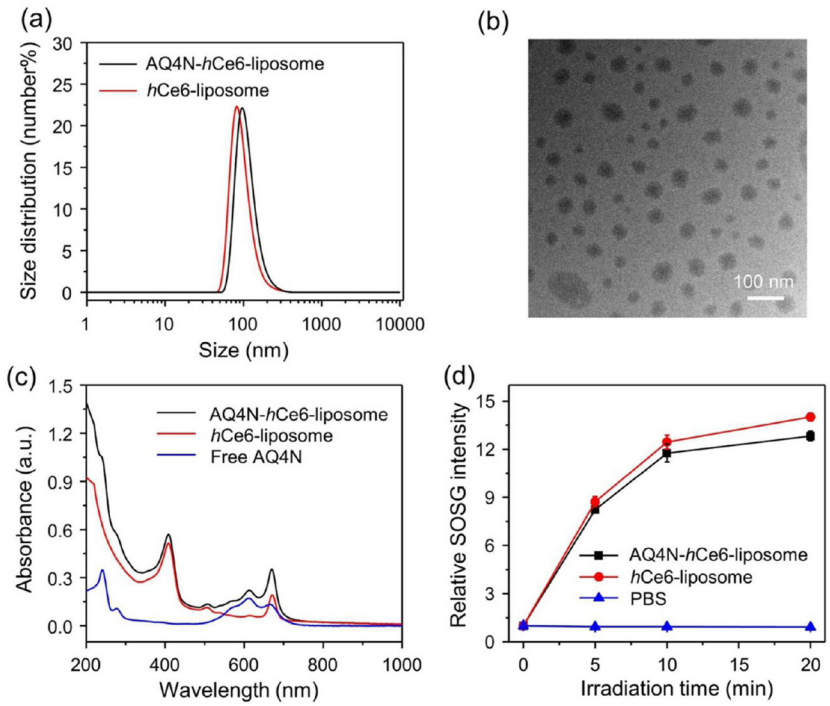


**Figure 2.**

Characterization of AQ4N-*h*Ce6-liposome. (a) DLS size distributions of AQ4N-*h*Ce6-liposome and plain *h*Ce6-liposome. (b) A TEM image of AQ4N-*h*Ce6-liposome. (c) UV–vis-NIR absorbance spectra of AQ4N-*h*Ce6-liposome, plain *h*Ce6-liposome, and free AQ4N. (d) Singlet oxygen generation abilities of AQ4N-*h*Ce6-liposome and plain *h*Ce6-liposome determined by using SOSG, whose recovered fluorescence indicated the generation of single oxygen. The concentration of *h*Ce6 was 5 $\mu$M in these experiments. The error bars were based on triplicate measurements.

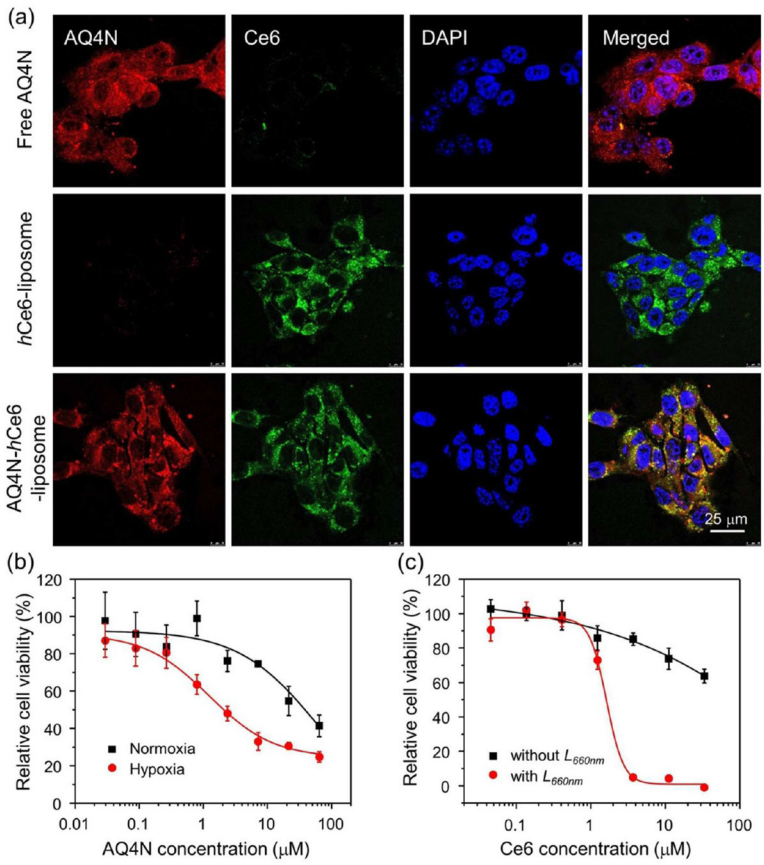


**Figure 3.**

Intracellular internalization and cytotoxicity of AQ4N-*h*Ce6-liposome. (a) CLSM observation of intracellular internalization profiles of AQ4N-*h*Ce6-liposome, plain *h*Ce6-liposome, and free AQ4N after incubation with 4T1 cells. DAPI, Ce6, and AQ4N were excited at 404, 488, and 633 nm, respectively. (b) Cytotoxicity of AQ4N-*h*Ce6-liposome to 4T1 cells under normoxia and hypoxia conditions measured by the standard MTT assay. The error bars were based on triplicate measurements. (c) Cytotoxicity of AQ4N-*h*Ce6-liposome to 4T1 cells in the presence or absence of 660 nm LED light irradiation recorded by the standard MTT assay. The error bars were based on triplicate measurements.

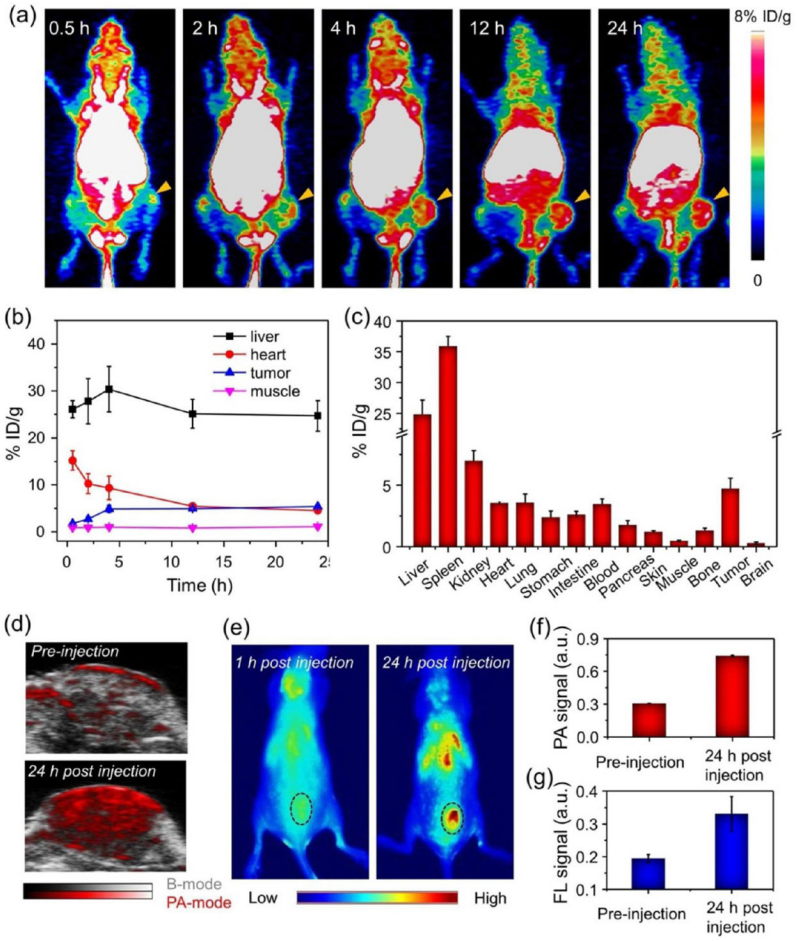


**Figure 4.**

*In vivo* multimodal imaging and pharmacokinetic behaviors of AQ4N-*h*Ce6-liposome. (a) PET images of 4T1 tumor-bearing mice with i.v. injection of $^{64}Cu^{2+}$-labeled AQ4N-*h*Ce6-liposome recorded at different time intervals p.i. The tumors are indicated with yellow arrows. (b) Quantification of AQ4N-$^{64}$Cu-*h*Ce6-liposome levels in the liver, heart, tumor, and muscle of 4T1 tumor bearing mice at various time points p.i. (c) Biodistribution of AQ4N-$^{64}$Cu-*h*Ce6-liposome in various organs and tissues of 4T1 tumor-bearing mice at 24 h p.i. as determined by $^{64}$Cu radioactivity measurement by a gamma counter. Error bars were based on the standard errors of the mean of triplicate samples. (d) PA imaging of tumor regions recorded before and 24 h post-i.v. injection of AQ4N-*h*Ce6-liposome. (e) Fluorescence imaging of 4T1 tumor bearing mice with i.v. injection of AQ4N-*h*Ce6-liposome at 1 and 24 h p.i. The tumors are indicated with black dashed circles. (f and g) Semiquantitatively analyzing the PA (f) and fluorescence (FL) signal (g) of AQ4N-*h*Ce6-liposome in tumors based on the images shown in (d and e). Error bars were based on triplicate measurements.

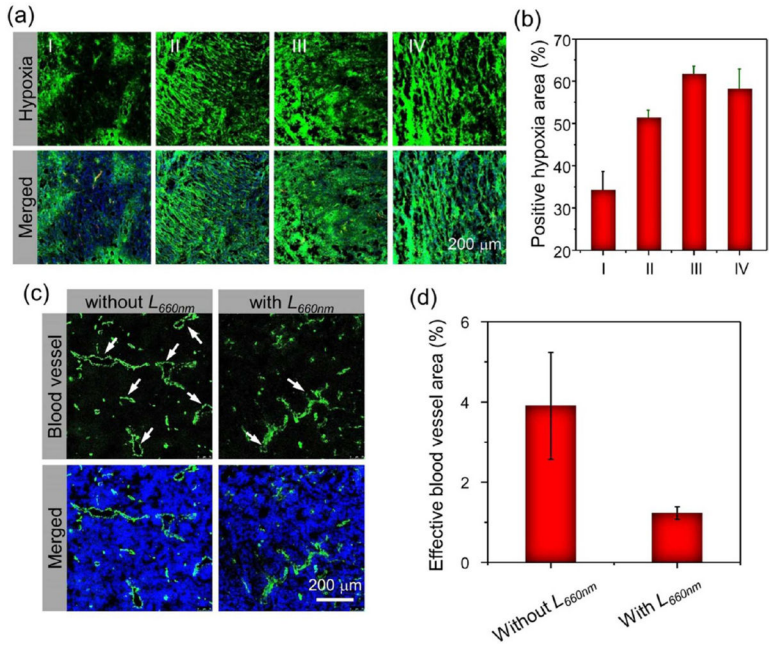


**Figure 5.**

Tumor hypoxia and blood vasculature evolutions induced by photodynamic treatment with AQ4N-*h*Ce6-liposome. (a) *Ex vivo* immunofluorescence staining of tumor slices collected from AQ4N-*h*Ce6-liposome injected mice with different treatments. (b) Semiquantitative analysis of the percentages of positive hypoxia regions before and after 660 nm LED light irradiation based on the images shown in (a). I, II, III, and IV stand for those tumors collected before and at 5 min, 4 h, and 24 h post-irradiation with 660 nm LED light (2 mW $cm^{-2}$, 1 h), respectively. (c) *Ex vivo* immunofluorescence staining showing the changes of blood vessels (green) in tumors collected from the 4T1-tumor bearing mice with i.v. injection of AQ4N-*h*Ce6-liposome before and at 4 h post-660 nm LED light irradiation (2 mW $cm^{-2}$, 1 h). (d) Semiquantitative analysis of the effective blood vessel areas, which appears as opened circles indicated with white arrows, in the slices shown in (c) using the Image-Pro Plus 6.0. software.

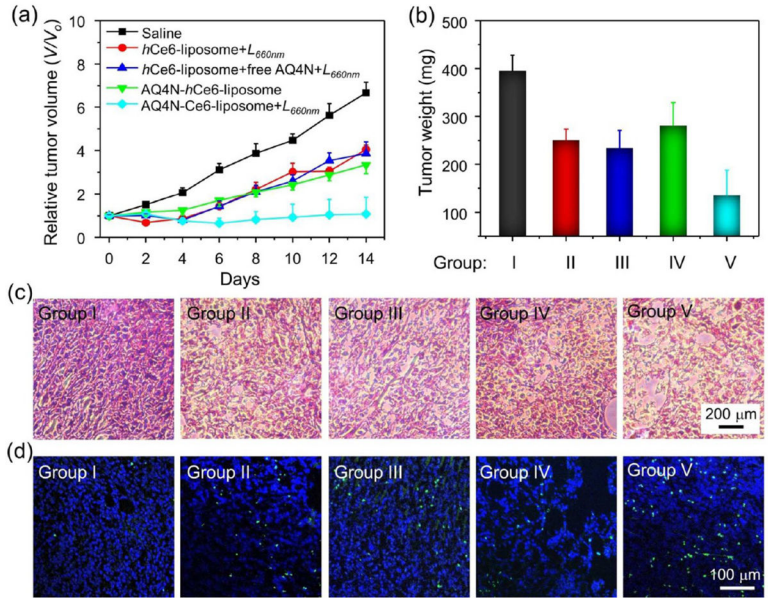


**Figure 6.**

*In vivo* cancer combination therapy with sequentially activated AQ4N-*h*Ce6-liposome. (a) Tumor growth curves of mice after various different treatments as indicated. $V$ and $V_o$ stand for the tumor volumes after and before the treatment, respectively. Error bars were based on five mice in each group. (b) Average tumor weights from different groups collected at 14 d after the treatment. (c and d) H&E (c) and TUNEL staining (d) of tumor slices collected from mice from various groups at 24 h post-660 nm LED light irradiation. Groups I, II, III, IV, and V stand for saline treatment (control), *h*Ce6-liposome + $L_{660\ nm}$, *h*Ce6-liposome + free AQ4N + $L_{660\ nm}$, AQ4N-*h*Ce6-liposome only, −and AQ4N-*h*Ce6-liposome + $L_{660\ nm}$ in (d–f), respectively. $L_{660\ nm}$ stands for 1 h irradiation with 660 nm LED light (2 mW cm$^2$).